



Cite this: *Energy Environ. Sci.*, 2021, 14, 2460

High output direct-current power fabrics based on the air breakdown effect†

Renwei Cheng,[‡] Kai Dong,[‡] Pengfei Chen,^{ab} Chuan Ning,^{ab} Xiao Peng,^{ab} Yihan Zhang,^{ab} Di Liu^{ab} and Zhong Lin Wang^{id*abc}

Energy-harvesting textiles based on triboelectric nanogenerators (TEGs) have attracted intense attention, due to their broad potential applications in wearable electronics. However, the bottlenecks of limited and alternating current electrical output have greatly hindered the development of textile TEGs. Here, by simply and easily coating two electrodes on the top side (breakdown electrode) and bottom side (friction electrode) of a polyester–cotton fabric, a light-weight, highly flexible and wearable fabric-based direct current TENG (FDC-TENG) with high power output is developed. Various structural parameters and environmental factors are thoroughly and systematically explored for comprehensive understanding of the FDC-TENG. The surface charges induced by triboelectrification can be unidirectionally and efficiently harvested through the conductive plasma channel caused by air breakdown, which endows the finger-sized FDC-TENG with the abilities to light up 99 bulbs and 1053 LEDs and drive watches and calculators easily and directly without rectifying or capacitor charging. This work may provide a paradigm shift for high output direct-current power fabrics and expand their scope for application in wearable electronics.

Received 7th January 2021,
 Accepted 10th March 2021

DOI: 10.1039/d1ee00059d

rsc.li/ees

Broader context

Fossil energy has promoted the development of human society. However, its unsustainability and pollution have forced humans to find new energy sources. Although it is difficult to replace high-power fossil energy in the near future, the reduction in the energy consumption of electronic equipment and the improvement in the performance of energy harvesting devices will benefit the wide application of new energy devices. The batteries or capacitors that are currently used in wearable electronics are restricted by their limited lifetime, replacement frequency, and environmental problems. However, some emerging energy harvesting technologies, such as thermoelectric generators and solar cells, are highly dependent on the environment. A fabric-based triboelectric nanogenerator (TENG) can convert human biomechanical energy into electricity, and seems to be an ideal energy source for wearable electronics. In this work, a fabric-based direct current TENG (FDC-TENG) which can provide high DC output was prepared. The finger-sized FDC-TENG can light up 99 bulbs and 1053 LEDs and drive watches and calculators easily and directly. Our systematic research presents that this high-power output, fully flexible, light weight, and wearable FDC-TENG may promote energy harvesting for wearable electronics.

Introduction

The rapid development of wearable electronic devices in the era of the Internet of Things (IoT) has greatly transformed and

enriched our lives. However, these electronic devices, no matter how smart or crucial, will lose their vitality after leaving the energy source. The currently used batteries or capacitors are unable to meet the future demands for sustainable and environment-friendly energy sources.^{1,2} Although some emerging energy harvesting technologies, such as thermoelectric generators and solar cells, can achieve short-term power supply, their high dependence on environmental conditions restricts their widespread application, especially for the owners of wearable electronics who usually stay indoors and in stable temperature environments.^{3,4} As a revolutionary energy harvesting technology, a triboelectric nanogenerator (TENG), which originates from Maxwell's displacement current and roots in the coupling effect of triboelectrification and electrostatic induction, can convert

^a CAS Center for Excellence in Nanoscience, Beijing Key Laboratory of Micro-Nano Energy and Sensor, Beijing Institute of Nanoenergy and Nanosystems, Chinese Academy of Sciences, Beijing 100083, China

^b School of Nanoscience and Technology, University of Chinese Academy of Sciences, Beijing 100049, China

^c School of Material Science and Engineering, Georgia Institute of Technology, Atlanta, Georgia 30332, USA. E-mail: zhong.wang@mse.gatech.edu

† Electronic supplementary information (ESI) available. See DOI: 10.1039/d1ee00059d

‡ R. Cheng and K. Dong contributed equally to this work.

widely distributed but always neglected mechanical energy into electricity.^{5–7} Owing to their low cost, light weight, environmental friendliness and diverse material options, TENGs have tremendous application prospects in micro/nano energy harvesting,^{8–10} active sensors,^{11–13} human–machine interfaces,^{14–16} blue energy harvesting,^{17–19} high voltage sources,^{20–22} *etc.*

Textiles are indispensable necessities in our lives, which have accompanied us for thousands of years. Fabric-based TENGs (F-TENGs), combining the energy harvesting and active sensing of TENGs as well as the flexibility and breathability of fabrics, have naturally been considered as one of the significant solutions for powering wearable electronics, by harvesting the most common dispersed and sustainable human motion energy,^{23–26} especially in the era of IoT, where sensors have the characteristics of low-power consumption and widely movable distribution.²⁷ However, the alternating current (AC) outputs of traditional F-TENGs do not match most of the electronic devices used in our daily life that require a direct current (DC) power supply. Therefore, it is imperative to try to convert AC into DC. Although some methods have been proposed to solve this issue for hard TENGs, such as novel structural design or selecting semiconductors as substrates,^{28,29} almost all of the researchers who focus on soft F-TENGs simply choose rectifiers to obtain DC output, due to the hindrance of the material properties of textiles.^{30–33} Undeniably, using a rectifier is the easiest and most convenient way. Nevertheless, as an electronic device, the rectifier will inevitably consume some power, and the consumption may even be comparable to target electronic devices. In addition, the volume of the rectifier cannot be ignored, which may restrict the wide application of some miniature TENGs for manufacturing micro-nano devices. Moreover, it seems inconvenient to add a rigid rectifier to a flexible F-TENG applied to wearable electronics. Recently, Chen *et al.* reported an F-TENG that can output DC without a rectifier based on the coupling effect of triboelectrification and air breakdown. However, the DC output is inseparable from the rigid acrylic substrate to keep the breakdown gap, which makes the soft textiles meaningless.³⁴ Furthermore, the output power of most F-TENGs is not high enough to drive most of the electronic devices. Therefore, energy harvesting textiles with high-power-output performance are still one of the major tasks that need to be solved urgently.^{7,35,36}

Herein, a high-power-output, fully flexible, light-weight, and wearable fabric-based DC TENG (FDC-TENG) is developed through an extremely simple preparation process, which can convert mechanical energy into high DC electrical output. The FDC-TENG only consists of a polyester–cotton fabric and two electrodes on its surface, including the breakdown electrode on the top side and the friction electrode on the bottom side. The friction electrode is used to generate triboelectric charges, which are efficiently harvested by the breakdown electrode through the conductive plasma channel resulting from air breakdown. Current and voltage are linearly related to the sliding speed, while it affects the charge transfer only at low speeds ($<0.05 \text{ m s}^{-1}$ in the work). The increase of relative humidity will seriously reduce the electrical output, due to the

dissipation of the surface charges on the tribo-materials. Moreover, the electrical output can be further improved by increasing the number of breakdown electrodes or integrated units. Due to the high DC electrical output of the FDC-TENG, wearable electronics, such as watches and calculators, can be continuously and directly driven by manually sliding a finger-sized FDC-TENG, which can also light up 99 bulbs and 1053 LEDs easily. Therefore, the developed FDC-TENG as an electronic textile with high-power DC output exhibits broad application prospects in wearable power textiles.

Results and discussion

Structural design and working mechanism

We consider that how to maintain a stable but tiny breakdown gap with soft textiles is the key to creating a DC output power fabric based on air breakdown. In this work, a breakdown electrode is prepared on the top side of a polyester–cotton fabric to achieve this goal, which takes advantage of the naturally thin feature of the textile substrate. The preparation of an FDC-TENG is very simple and easy. The three-dimensional schematic illustrated in Fig. 1a shows that the FDC-TENG consists of only a fabric substrate and two electrodes. The bottom friction electrode acts as a tribo-material to generate triboelectric charges through the triboelectrification effect. The top breakdown electrode harvests these triboelectric charges through the conductive plasma channel created by air breakdown. A polyester–cotton fabric is selected as the substrate, owing to the combination of the high strength of polyester and the high air permeability of cotton. Benefitting from the excellent conductivity and the strong tendency to lose electrons, silver paste is chosen to fabricate the breakdown electrode and the friction electrode. It is necessary to brush the two electrodes without overlapping to avoid any short circuit. The outstanding conductivities of the breakdown electrode and friction electrode are displayed in Fig. S1 (ESI[†]). The backside resistance at the diagonal of a $1.5 \times 2 \text{ cm}^2$ polyester–cotton fabric coated with silver paste is as high as $103 \text{ T}\Omega$. Therefore, the backside is not conductive, and the silver paste does not penetrate to the reverse side of the fabric. A polyester–cotton fabric coated with silver paste is placed on a mechanical linear motor and slides on an FEP film at a frequency of 1 Hz for 10 hours (mass = 2 kg). It can be seen from Fig. S2 (ESI[†]) that neither the relative mass nor the relative electrical conductivity shows significant reduction even after 10 hours of continuous friction. Therefore, the silver electrode shows robust adhesion with the fabric, and the conductivity will not decrease noticeably after sliding for a long time. In addition, the fabric substrate endows the FDC-TENG with naturally high flexibility, light weight (15.68 mg cm^{-2}), and thin thickness ($170 \text{ }\mu\text{m}$) (Fig. S3, ESI[†]). Fig. 1b depicts the actual photographs of the top side and bottom side of the FDC-TENG.

As shown in Fig. S4a (ESI[†]), the FDC-TENG is thrown into a beaker with water and stirred at a speed of 300 rpm. The variations of the relative electrical output and the relative mass with washing time are shown in Fig. S4b (ESI[†]). It turns

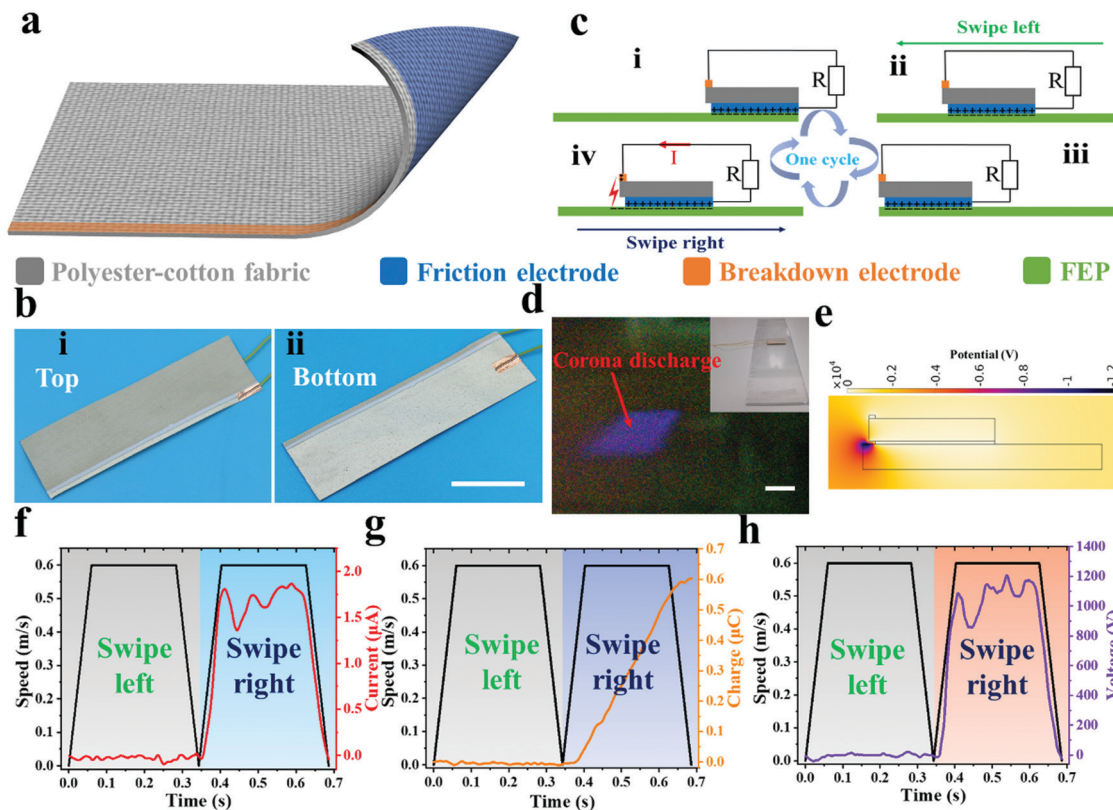


Fig. 1 Structure and working mechanism of the FDC-TENG. (a) Schematic illustration of the FDC-TENG. (b) Photographs of an actual FDC-TENG, including the top side (bi) and the bottom side (bii) (scale bar: 1 cm). (c) Schematic of the working mechanism of the FDC-TENG with four states in one cycle. (d) The glow of corona discharge caused by the air breakdown between the breakdown electrode and the FEP film (scale bar: 2 cm). (e) The potential distribution of the FDC-TENG obtained by finite element simulation through COMSOL software. (f–h) The relationships between the current (f), charge transfer (g), and voltage (h) and the sliding speed of the FDC-TENG in part c.

out that both of them can be well maintained without significant degradation even after washing for 20 h. Therefore, the FDC-TENG shows excellent washing durability. The air permeabilities of polyester–cotton fabrics coated with and without silver paste under different differential pressures are shown in Fig. S5 (ESI†). It can be found that the air permeability improves with the increase in pressure difference. Although silver paste has a significant effect on air permeability, the polyester–cotton fabric coated with silver paste still has good breathability.

The working mechanism of the FDC-TENG in the contact-sliding mode based on air breakdown is illustrated in Fig. 1c, which can be divided into four stages in one cycle. A fluorinated ethylene propylene (FEP) film is chosen as the friction layer to obtain high surface charge density. To analyze the mechanism in more detail, we assign the sliding distance, maximum speed, acceleration, and deceleration to 17 cm, 0.6 m s^{-1} , 10 m s^{-2} , and -10 m s^{-2} , respectively. The speed and corresponding electrical output values are shown in Fig. 1f–h. In the initial state, the FDC-TENG and the FEP film are aligned right. The surfaces of the FEP film and the friction electrode will be charged with the same number of opposite charges caused by the triboelectrification effect. And the FEP film is negatively charged due to its stronger electron trapping capability (Fig. 1ci). Afterwards, when the FDC-TENG moves from the

right end to the left, the surface charge density of the FEP film on the left-hand side of the breakdown electrode is not high enough to break down air. Thus, there will be no output in the external circuit (Fig. 1cii and ciii). The corresponding current, charge transfer and voltage values are shown in the left part of Fig. 1f–h, respectively. When the FDC-TENG moves from the left end to the right, the FEP film can hold quasi-permanent triboelectric charges since it is an electret. Therefore, a high electrostatic field will be built on the surface of the FEP film on the left-hand side of the breakdown electrode. Once the strength of the electrostatic field is higher than that of the critical breakdown electric field of air ($\sim 3 \text{ kV mm}^{-1}$ according to Paschen's law), the gas molecules in the air will be ionized into plasma, which causes the insulated air to become a conductor. Large quantities of electrons will unidirectionally transfer from the surface of the FEP film to the breakdown electrode *via* the conductive plasma channel, and ultimately flow to the friction electrode through the external circuit (Fig. 1civ). The corresponding current, charge transfer, and voltage values in this stage are shown in the right part of Fig. 1f–h, respectively. It can be found that the output curves are highly consistent with the speed curves. And an approximate constant current or voltage can be obtained when the FDC-TENG is moved at a fixed speed. The photograph of the glow of corona

discharge that resulted from the air breakdown when sliding the FDC-TENG on the FEP film is displayed in Fig. 1d. The surface potential of the FEP film is also measured (Fig. S6, ESI†). It is obvious that the surface potential is significantly reduced after sliding the FDC-TENG to the right-hand side of the FEP film, indicating that some surface charges of the FEP film are discharged by air breakdown. A simulation by finite element simulation using COMSOL Multiphysics is presented in Fig. 1e for a more quantitative understanding of the potential distribution.

It is worth noting that the polyester-cotton fabric only acts as the substrate of the FDC-TENG, which can be replaced with any thin solid material. Here, we verify this with different fabrics and films. As for the fabrics, the electrical output of the FDC-TENG with cotton fabric as the substrate, which has the same thickness as polyester-cotton fabric (0.15 mm), has been investigated (Fig. S7a, ESI†). The consistent electrical outputs of the two materials indicate that the substrate material has little effect on the electrical output. Moreover, the nylon fabric-based FDC-TENG also exhibits high output, indicating a wide selection of fabric materials. Some fabrics with different thicknesses and different roughnesses as substrates have also been investigated. The electrical output decreases as the thickness of the polyester fabric increases, which may be attributed to the increase of the breakdown gap (Fig. S7b, ESI†). The cotton fabric with different roughnesses on the front side and back side is selected as the substrate to study the effect of roughness. The electrical output of the cotton fabric when the front side and back side are coated with silver paste as the friction electrode separately is shown in Fig. S7c (ESI†). The surface charges of the FEP film may have reached saturation. Therefore, the FDC-TENGs with different roughnesses of the friction electrode exhibit similar electrical output performance. As for the films, the electrical outputs of the FDC-TENGs based on polytetrafluoroethylene (PTFE), polyimide (PI), FEP, and nylon films as substrates are shown in Fig. S7d (ESI†). The thickness of all the films is 0.1 mm. It turns out that the different film materials also have little effect on the electrical output. These results indicate that flame-retardant materials can also be selected as substrates to enable FDC-TENGs to exhibit fire-proof performance.

The generated charge density after the friction electrode slides and the residual charge density after the breakdown electrode slides on the FEP film are measured as $128.14 \mu\text{C m}^{-2}$ and $40.94 \mu\text{C m}^{-2}$, respectively (Fig. S8a, ESI†). The schematic diagram of the measurement methods and its details are provided in Fig. S9 and Note S1 (ESI†) respectively. Moreover, under the same weight, the charge transfer of the FDC-TENG with a charge collection area of $14 \times 5 \text{ cm}^2$ is shown in Fig. S8b (ESI†). The harvested charge density is $79.77 \mu\text{C m}^{-2}$. Therefore, the charge collection efficiency is 62.25%. Efficient collection of surface charges is achieved. It is worth noting that the number of generated charges is greater than the sum of harvested charges and residual charges, which may be attributed to the charge dissipation.

In-depth understanding of the FDC-TENG

To optimize the electrical output performance of the FDC-TENG, the influences of structure parameters are systematically

investigated, including the length of the breakdown electrode (denoted A), the height of the breakdown electrode from the surface of the friction layer (denoted B), the width of the breakdown electrode (denoted C), the sliding distance of the FDC-TENG (denoted D), the width of the friction electrode (denoted E), and the length of the friction electrode (denoted F), as shown in Fig. 2a. The electrical outputs, including short-circuit current (I_{SC}), short-circuit charge transfer (Q_{SC}), and voltage, are measured using a mechanical linear motor. It is worth noting that the ultrahigh voltage of the FDC-TENG is measured using an oscilloscope with a high-voltage probe (HVP 3015, 1/1000, 500 M Ω), which cannot be regarded as the open-circuit voltage due to the huge inherent resistance of the FDC-TENG. The influence of C on the electrical output performance has been thoroughly studied, and the variation of I_{SC} is shown in Fig. 2b. There are two phenomena that need attention. Firstly, the peak of I_{SC} hardly changes with C , which may be attributed to the unchanged maximum sliding speed (the effect of the sliding speed on I_{SC} will be discussed later). The second phenomenon is that a reverse current appears and increases with the increase of C . First of all, it is significant to investigate the causes of the reverse current. By matching the current curve and speed curve when $C = 2 \text{ cm}$, it can be found that the reverse current appears in the initial period when the FDC-TENG slides from the right end to the left (Fig. 2c). The working mechanism of the FDC-TENG with a large C is shown in Fig. S10 (ESI†), and the whole process is analyzed in Note S2 (ESI†). Here, we focus on analyzing the stages of Fig. S10iv and v (ESI†) to elaborate the formation of the reverse current in detail. When the FDC-TENG slides to the right, there are electrons with a density of σ_2 on the FEP film directly under the breakdown electrode. These electrons will generate a strong electrostatic field with an ability to cause air breakdown. However, the existence of a solid polyester-cotton fabric results in a large critical breakdown field strength between the FEP film and the breakdown electrode, which is larger than the electrostatic field strength generated by σ_2 . Therefore, in this area, the surface charges on the FEP film will not be harvested. However, for the charges on the FEP film on the left-hand side of the breakdown electrode, there will be no interference from the polyester-cotton fabric. The air breakdown can occur normally and some of the surface charges will be harvested. We denote the surface charge density after being harvested as σ_1 . Thus, the absolute value of σ_2 is greater than that of σ_1 in Fig. S10iv (ESI†). When the FDC-TENG slides from the right end to the left, the breakdown electrode will move from the area with high surface charge density (σ_2) to that with low density (σ_1) (Fig. S10v, ESI†). The induced positive charges on the breakdown electrode correspondingly decrease as the sliding distance increases. A reverse current (I_{B}) will flow from the breakdown electrode to friction electrode in the external circuit, which is opposite to the direction of the current I_{A} generated by air breakdown. It is worth noting that when C is small, such as 0.1 cm, the reverse current will be so tiny that the electrical output can be regarded as DC (Fig. 2b). As for the FDC-TENG with a large C , assuming that the reverse current disappears when it moves from the right end to the left by a distance of ΔX , which can be

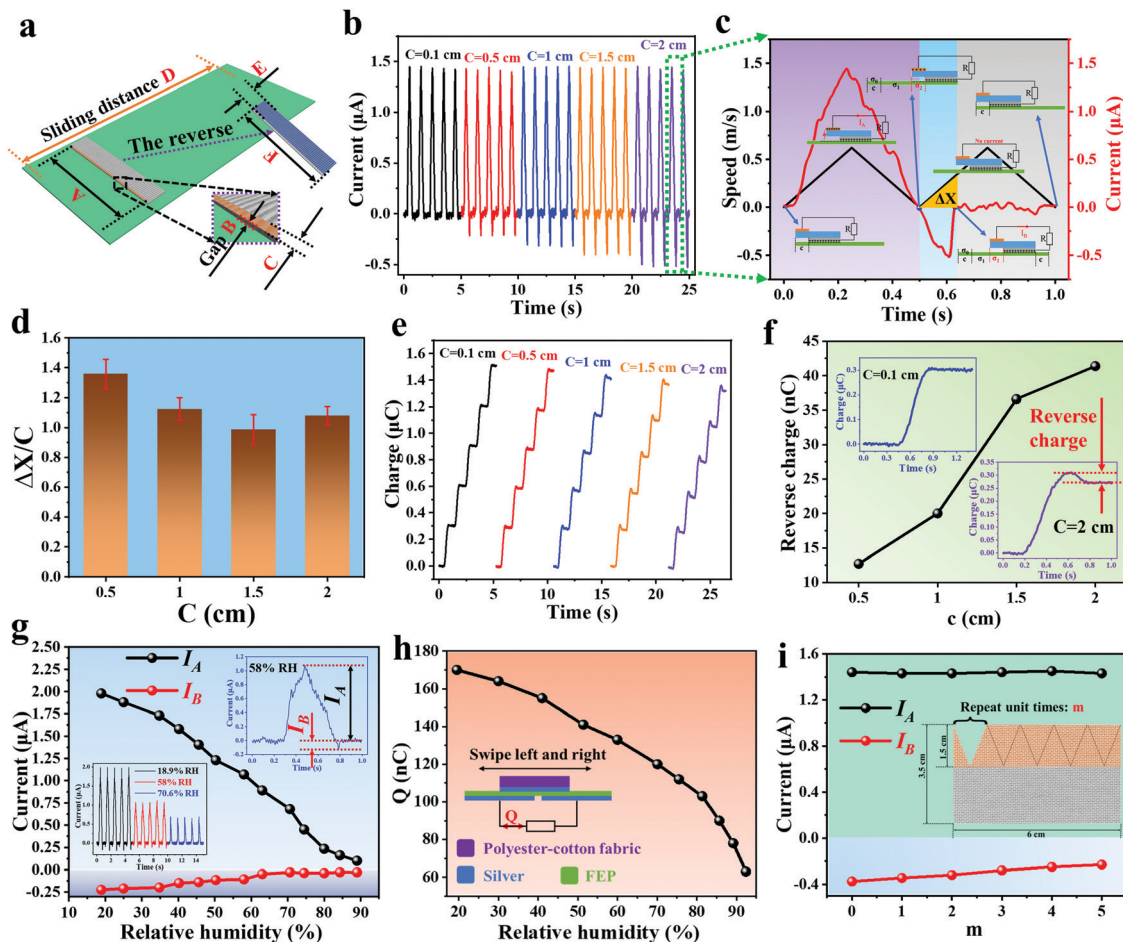


Fig. 2 Output performance of the FDC-TENG with reverse current/charge. (a) Some structural parameters to be studied in this work, including the length of the breakdown electrode (denoted A), the height of the breakdown electrode from the surface of the friction layer (denoted B), the width of the breakdown electrode (denoted C), the sliding distance of the FDC-TENG on the friction layer (denoted D), the width of the friction electrode (denoted E), and the length of the friction electrode (denoted F). (b) The current of the FDC-TENG with different C values. (c) The sliding state and the corresponding current of the FDC-TENG when C is 2 cm. (d) The variation of $\Delta X/C$ with C . (e) The charge transfer of the FDC-TENG with different C values. (f) The relationship between the reverse charge and C . The charge transfer of the FDC-TENG when $C = 0.1$ cm is presented in the top-left corner, while the definition of the reverse charge is shown in the bottom-right corner. (g) I_A and I_B of the FDC-TENG for different RH values. The definition of I_A and I_B and the current under 18.9%, 58%, and 70.6% RH are displayed in the top-right corner and bottom-left corner, respectively. (h) The relationship between the charge transfer and humidity when the friction electrode slides on the FEP film. (i) Comparison of the current of the FDC-TENG when changing the shape of the breakdown electrode.

expressed as

$$\Delta X = \frac{1}{2} a \cdot \Delta t^2 \quad (1)$$

where a and Δt are the sliding acceleration and duration of the reverse current, respectively. It can be seen from Fig. 2d that all $\Delta X/C$ values are close to 1, which verifies the above explanation. Similar results appear in reverse charge (Fig. S11, ESI†). The slight deviation of the FDC-TENG with $C = 0.5$ cm may be attributed to the relatively large experimental error. As the width of the breakdown electrode increases, more induced charges are generated. Thus, the reverse current will increase accordingly with the increase of the breakdown electrode width (Fig. 2b). In addition, as shown in Fig. 2e and f, there is also an increased reverse charge with the increase of C , which in turn results in a slightly decreased Q_{SC} . It is worth mentioning that

the reverse charge when $C = 0.1$ cm is not included in Fig. 2f, because it is too small to calculate in the measured transfer charge curve (inset in the top-left corner of Fig. 2f). Moreover, the voltages of the FDC-TENG with different C values are similar, as demonstrated in Fig. S12 (ESI†).

The influence of the air pressure and temperature on the DC-TENG based on air breakdown was systematically investigated in a previous report.³⁷ However, relative humidity (RH) was not involved. It is well known that the air breakdown phenomenon will occur more easily when the air is drier. Therefore, the RH may have a significant impact on the electrical output of the FDC-TENG. As depicted in Fig. 2g, both the absolute values of I_A and I_B decrease with the increase of RH. The I_B is only determined by the surface charge density under the consistent experimental conditions except for RH; thus, the decreased I_B indicates the reduced surface charge density of the FEP film.

According to previous reports,^{38,39} there will be a water layer on the surfaces of the tribo-materials as the RH increases, which will aggravate the dissipation of the surface charges. The induced charges harvested using TENGs can reflect the surface charge density generated by the friction of two materials.^{40,41} To this end, we design a freestanding triboelectric-layer mode TENG to further verify the variation of surface charges of the FEP film after rubbing with the friction electrode under different RHs. From Fig. 2h, it is clear that the increased RH will reduce the transferred charge (Q), denoting the fact that the surface charge density of the FEP film decreases with larger RH again. Therefore, the decrease of the surface charge density of the FEP film is one of the reasons for I_A and I_B tending to 0 μA as the RH increases. Moreover, the increase of RH will also increase the critical breakdown electric field for air breakdown, which in turn results in a reduced I_A .⁴² The current output performance of the FDC-TENG with different breakdown electrode shapes is measured by cropping the breakdown electrode rationally, as schematically shown in the inset of Fig. 2i. It's worth noting that a long C chosen deliberately will highlight the influence of the breakdown electrode shape on the output performance. However, it will inevitably result in an obvious I_B . The I_A exhibits no noticeable relationship with the breakdown electrode shape and remains at $\sim 1.43 \mu\text{A}$, while I_B tends to 0 μA when cropping more area of the breakdown electrode. This indicates that the breakdown electrode shape will affect the reverse current but not the air breakdown. Moreover, we find that the output will be enormously affected when the back side of the friction layer is covered with a conductor. As the distance between the upper surface of the FEP film and the conductor (defined as h) increases, the current output increases first and finally stabilizes (Fig. S13a, ESI†). The conductor will have a shielding effect on the surface charges of the FEP film, which will reduce the surface potential and further lessens the electrostatic field strength between the FEP film and breakdown electrode (Fig. S13b, ESI†). The increase of h will weaken the shielding effect. Furthermore, it can be ignored when h is large enough, which is 2.6 mm in this work. This phenomenon shows that one of the necessary conditions for the DC-TENG based on air breakdown is that the friction layer should be far away from the irrelevant conductor.

Structure optimization and electrical output performance of the FDC-TENG

The interference of I_B to the DC output can be eliminated by reducing C . Therefore, C is controlled to 0.1 cm in the following studies. It is observed that the electrical output seems to be highly correlated with the speed according to the earlier results in Fig. 1f–h. Here, the relationship between them is systematically studied. The I_{SC} , voltage, and Q_{SC} values of the FDC-TENG at different speeds are shown in Fig. 3a–c, respectively. The I_{SC} and voltage nearly increase with speed linearly, which reveals that speed has a significant impact on I_{SC} and voltage. In addition, the super-linear relationships between I_{SC} /voltage and speed can also be further exploited for speed sensing. The increase of speed will scale up the Q_{SC} when the FDC-TENG slides with a speed lower

than 0.05 m s^{-1} , while it remains almost unchanged at a higher speed. The relationships of the surface potential of the FEP film with time and sliding speed have been investigated (Fig. S14, ESI†). It can be found in Fig. S14a (ESI†) that the surface potential of the FEP film decreases slightly with time, and decreases by only 1.16% in two minutes. However, compared with the saturated state, the harvested charges are reduced by about 26.9% at a sliding speed of 0.01 m s^{-1} (Fig. 3c). These results indicate that the charge dissipation is one of the reasons but not the key reason for the decrease of the harvested charges at low speeds. The charges on the surface of the FEP film after the friction electrode slides are the generated charges, and their variation can be expressed by that of the surface potential of the FEP film. Hence, the surface potential of the FEP film after the friction electrode slides at different speeds is further measured (Fig. S14b, ESI†). It turns out that the relationship between the surface potential and sliding speed is similar to that between the harvested charges and sliding speed in Fig. 3c. Moreover, the relative reduction in surface potential is almost equivalent to that in harvested charges. Therefore, the decrease in generated charges at low speeds is the key reason for the decrease of the harvested charges at low speeds. More importantly, as illustrated in the insets of Fig. 3a and b, the FDC-TENG can provide an approximately stable current or voltage when the speed remains constant, which is friendly for powering electronic devices. The average energy conversion efficiencies at different sliding speeds are shown in Fig. S15 (ESI†). The details of the calculation method are analyzed in Note S3 (ESI†). It can be found that the average energy conversion efficiency η of the FDC-TENG increases with the increase of sliding speed. And η reaches 0.35% at a sliding speed of 1 m s^{-1} . It is worth explaining that although the peak conversion efficiency is high in many studies, the average energy conversion efficiency of the TENG is usually no more than 10%.^{43–45} However, the relatively lower average energy conversion efficiency of our FDC-TENG may be attributed to the frictional energy loss at the contact interface. The increased acceleration and deceleration are conducive to the increase of I_{SC} and voltage, while the Q_{SC} is nearly invariant (Fig. S16, ESI†). The maximum speed increases with the increase of acceleration and deceleration when the sliding distance is constant, which will result in an increased I_{SC} and voltage. Nevertheless, the variations of acceleration and deceleration have little effect on the charge collection, wherefore the Q_{SC} will be changeless. Moreover, as the weight added onto the FDC-TENG increases, the electrical output increases initially, followed by reaching an approximate constant (Fig. 3d). A heavier weight will be beneficial to improving the effective contact area between the friction electrode and the FEP film, which will create more triboelectric charges on the FEP film and further increases the electrical output. However, the effective contact area will hardly increase when the weight is large enough, wherefore the electrical output will stop increasing. As the weight increases, I_B will become obvious and can be calculated when the loading weight is not lower than 1 kg, which increases first and then remains almost unchanged in the weight range of 1–3 kg (Fig. S17, ESI†). From Fig. 2, it is known that I_B is greatly affected by the surface charge density of the FEP film. Therefore, the variation of I_B is the

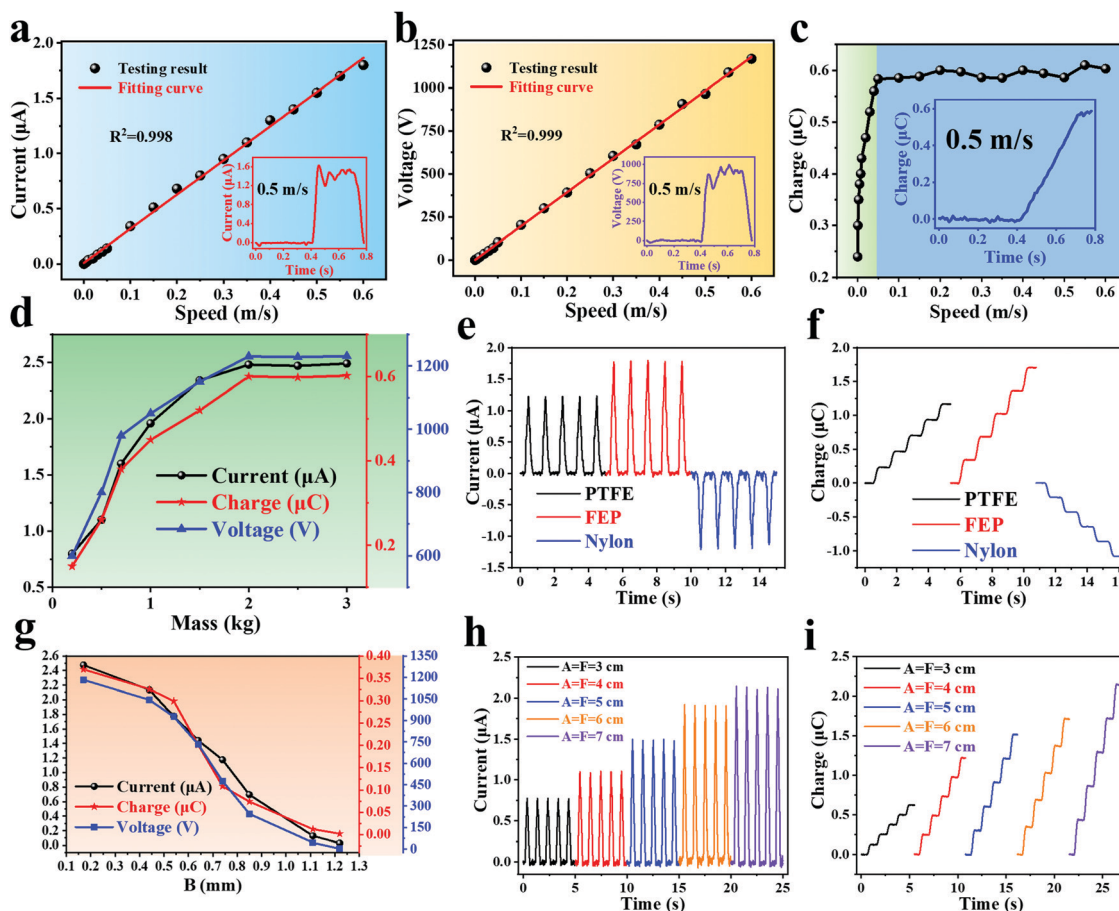


Fig. 3 Electrical output performance of the FDC-TENG. (a–c) The current (a), voltage (b), and charge transfer (c) at different speeds, and the insets show the output waveforms at 0.5 m s^{-1} . (d) Variation of the output performance of the FDC-TENG when adding different weights. (e and f) The current (e) and charge transfer (f) when sliding the FDC-TENG on PTFE, FEP, and nylon. (g) Effect of B on the electrical output performance. (h and i) The current (h) and charge transfer (i) of the FDC-TENG with different A and F ($A = F$) values.

strong evidence for the explanation about the influence of weight on the electrical output. Moreover, it is worth noting that the reverse current not only is 5.9% of the DC current even with a weight of 3 kg, but also exists briefly during the sliding process. These indicate that I_B still has little interference in DC output after adding a heavy weight. In addition, the long-term stability of the FDC-TENG is investigated, the I_{SC} displays no significant drop during one month of intermittent loading (Fig. S18, ESI†). It is worth noting that there is no significant change in the RH during the test, which is in the range of 34–41%.

Considering that the electrical output of the FDC-TENG derives from the surface charges of the friction layer, the selection of the material for the friction layer is extremely important. As presented in Fig. 3e and f, when the nylon fabric is selected as the friction layer, the direction of the current and the kind of harvested charge are both opposite to those of the FEP and PTFE films. This is attributed to the strong ability to lose electrons of nylon and the outstanding electron capture ability of PTFE and FEP. The voltage also demonstrates similar results when the FDC-TENG slides on these three friction materials (Fig. S19, ESI†). The wide selectivity of

the materials for the friction layer also illustrates the excellent adaptability of our FDC-TENG. In addition, the sliding distance D is also a crucial factor affecting electrical output. The increase of D will improve the Q_{SC} , I_{SC} and voltage due to the enlarged charge collection area and the increased maximum sliding speed (the frequency is maintained at 1 Hz) (Fig. S20, ESI†).

The breakdown electrode and friction electrode are two pivotal components of the FDC-TENG. To optimize the electrical output, the lengths and widths of these two electrodes as well as the breakdown gap between the breakdown electrode and FEP film are systematically studied. Air breakdown occurs in the gap between the breakdown electrode and FEP film; thus the gap distance B is an extremely important structural parameter. From Fig. 3g, it can be seen that the I_{SC} , Q_{SC} , and voltage of the FDC-TENG decrease as B increases. The increased B will reduce the intensity of the electrostatic field in the gap under a constant surface potential of the FEP film, which is not helpful for electrical output. Moreover, it can be found that there is almost no electrical output when the breakdown gap reaches 1.22 mm, which means that air breakdown no longer occurs in this air breakdown gap. The influence of the width of

the breakdown electrode C has been discussed in detail earlier. The relationship between the length of the breakdown electrode A and the electrical output is displayed in Fig. S21 (ESI[†]). The increased A is beneficial for the electrical output, which is attributed to the larger charge collection area. In addition, as for the width E and length F of the friction electrode, the electrical output increases with the decrease of E or F (Fig. S22 and S23, ESI[†]). When the force applied on the FDC-TENG remains constant, the intensity of the pressure at the contact surface of the friction electrode and FEP film will decrease with the increase of E or F , which will reduce the effective contact area between them and further reduce the electrical output.⁴⁶ The aforementioned results show that the effects of A and F on electrical output are opposite; thus we investigate their combined effects on electrical output to discuss which of them has more severe impact. As depicted in Fig. 3h and i, the electrical output of the FDC-TENG increases with the increase of A and F ($A = F$), which indicates that the charge collection area plays a more significant role in the electrical output. The variation of voltage also reveals a similar conclusion (Fig. S24, ESI[†]).

Improving the electrical output by optimizing the structure

Here, two methods are proposed to further improve the output of the FDC-TENG by ameliorating the structure. There are two sliding processes in each cycle. However, only one of them can output electrical power in all the above studies. Arranging another breakdown electrode on the opposite edge of the FDC-TENG can solve this issue, as schematically shown in Fig. 4a1. The two breakdown electrodes will alternately harvest the charges from the FEP film (Fig. 4a2 and a3). The detailed working mechanism is shown in Fig. S25 and described in Note S4 (ESI[†]). It is clear that the electrical output is doubled when both of the two breakdown electrodes are connected with the friction electrode (Fig. 4b and c and Fig. S26, ESI[†]). Fig. S27 (ESI[†]) depicts the charging curves of 33 μF electrolytic capacitors, where the capacitor can be charged to 2.38 V and 5.07 V within 90 s by the FDC-TENG with a single breakdown electrode and two breakdown electrodes, respectively. Moreover, the electrical outputs of a $4 \times 4 \text{ cm}^2$ FDC-TENG with 4 breakdown electrodes on the four edges in different sliding directions are shown in Fig. S28b (ESI[†]). The schematic

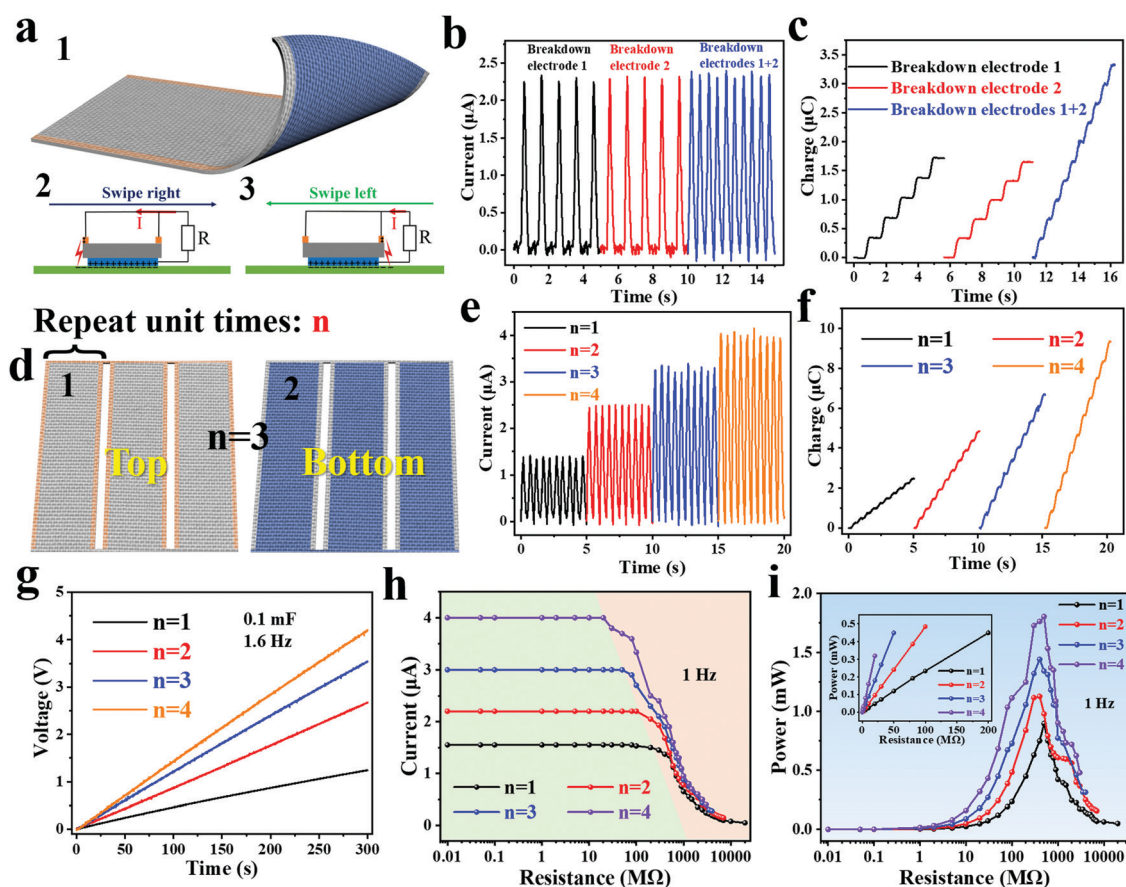


Fig. 4 The methods to increase electrical output by optimizing the structure. (a) Schematic illustration of the FDC-TENG with two breakdown electrodes (a1). Schematic diagrams when the FDC-TENG swipes right (a2) and left (a3). (b) and (c) The current (b) and charge transfer (c) of the FDC-TENG with two breakdown electrodes in different connection modes. (d) The diagrams of the top side (d1) and bottom side (d2) of the FDC-TENG when $n = 3$. (e) and (f) Effect of the number of integrated units n on the electrical output performance including the current (e) and charge transfer (f) of the FDC-TENG. (g) Charging voltage curves of the FDC-TENG for a 0.1 mF electrolytic capacitor with different n values at 1.6 Hz. (h) and (i) Variations of the output current (h) and power (i) with external resistance for different n values.

diagram of the sliding direction is displayed in Fig. S28a (ESI[†]). There is high electrical output in different sliding directions, indicating that the preparation of breakdown electrodes on the four edges of the FDC-TENG is effective for harvesting multi-directional energy. Furthermore, the electrical output for $\theta = 30^\circ$ and 45° is slightly higher than that for $\theta = 0^\circ$ and 90° , which may be attributed to the larger collection area. In addition, higher electrical output can be obtained by integrating multiple FDC-TENGs (the area of each integrated unit is $1.5 \times 5 \text{ cm}^2$). The diagrams of the top and bottom of the multiple integrated FDC-TENG are shown in Fig. 4d1 and d2, respectively. Fig. 4e and f show that a higher electrical output can be obtained with more integrated units. Furthermore, a similar result occurs when one of the two adjacent breakdown electrodes is removed, which indicates that one breakdown electrode can also simultaneously harvest the charges on the FEP film generated from the adjacent repeating units (Fig. S29, ESI[†]). Fig. 4g displays the voltage curves of an electrolytic capacitor with a capacitance of 0.1 mF charged directly using the FDC-TENG with different numbers of integrated units n at a sliding frequency of 1.6 Hz. It is noteworthy that no rectifier is

used during charging the capacitors. The charging rate increases with the increase of integrated units, indicating that increasing n is also a useful way to improve the output performance of the FDC-TENG. The voltage curves of different capacitors (0.22 mF, 0.33 mF, and 0.47 mF) charged by the FDC-TENG with $n = 4$ have also been tested, as shown in Fig. S30 (ESI[†]). As the capacitance increases, the charging voltage decreases with a reduced charging speed. And the electrolytic capacitor of 0.22 mF can be charged to 1.52 V within 240 s at 1.6 Hz. The output current I is measured by connecting with various resistances R in series at a frequency of 1 Hz and a sliding distance of 14 cm. $P = I^2R$ is used to calculate the power of the FDC-TENG. Fig. 4h shows that I remains almost stable when the resistance does not exceed 200 M Ω , 100 M Ω , 50 M Ω , and 20 M Ω with $n = 1, 2, 3,$ and 4 , respectively. The corresponding output power is displayed in the inset of Fig. 4i, and nearly increases with R linearly. This indicates that the FDC-TENG can be regarded as a constant DC power supply within the corresponding resistance range. Moreover, it is found that the electrical output of the FDC-TENG increases with the increase of n , and the maximum peak output power can reach 1.8 mW at

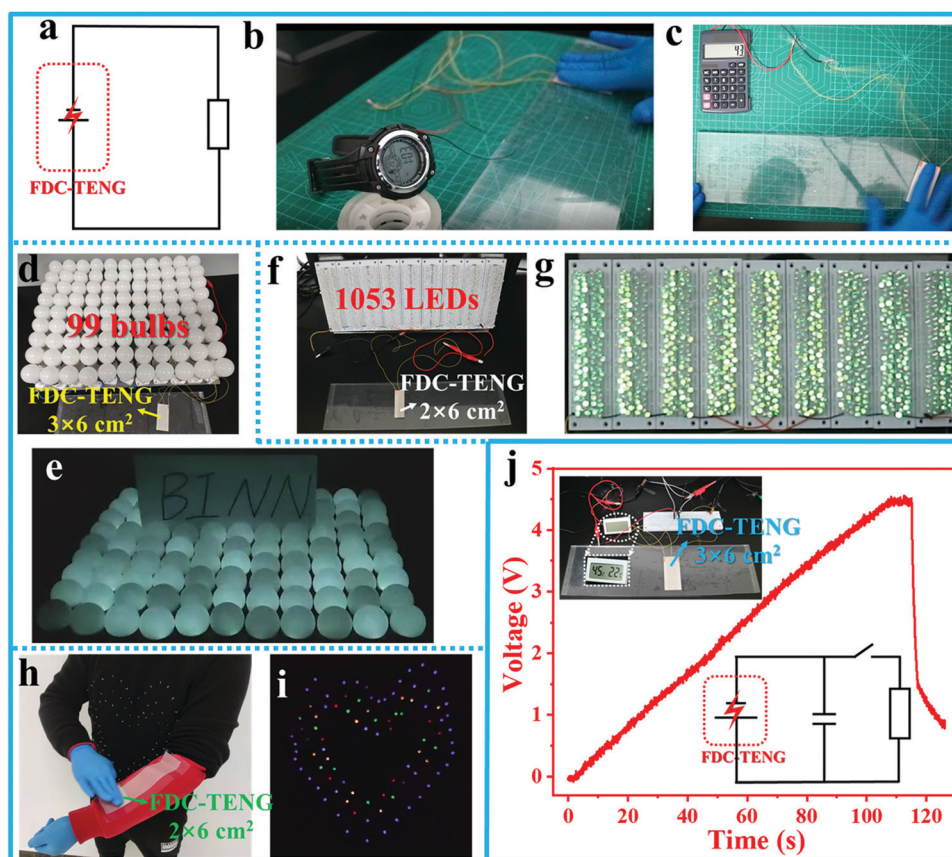


Fig. 5 Energy harvesting capability of the FDC-TENG. (a) Circuit diagram of an FDC-TENG to power electronics directly. (b and c) Photographs of a watch (b) and a calculator (c) directly driven using a $3 \times 6 \text{ cm}^2$ FDC-TENG. (d and e) Photographs of 99 bulbs lit up using an FDC-TENG, including the overall photo (d) and the word "BINN" visible after being illuminated with 99 bulbs (e). (f and g) Images of 1053 LEDs lit up using the FDC-TENG, including the overall photo (f) and the 1053 lighted LEDs (g). (h) Photograph taken when sliding the FDC-TENG on the FEP film attached to the arm to light up the heart-shaped colored lights. (i) Image of the lighted heart-shaped colored lights. (j) Charging curve of two $100 \mu\text{F}$ capacitors in series when a hygrothermograph is driven using the FDC-TENG; the insets show the overall image and the circuit diagram.

an external load resistance of 500 M Ω and a frequency of 1 Hz when $n = 4$.

Applications of FDC-TENGs to drive electronics

As for the traditional AC-TENG, a rectifier is required to convert AC to DC to drive electronic devices, which not only affects convenience and flexibility, but also consume the energy harvested by the AC-TENG. As shown in Fig. S31 (ESI[†]), the output will be reduced by 10.6% when a rectifier (the model is DB 107) is used. The high DC output of our FDC-TENG enables it to directly drive small electronic devices with neither an energy storage unit nor a rectifier. Fig. 5a depicts the circuit diagram of an electronic device directly driven using the FDC-TENG. The corresponding photographs of an electronic watch and a commercial calculator directly driven using a FDC-TENG with an area of only $3 \times 6 \text{ cm}^2$ are shown in Fig. 5b and c. By manually sliding the FDC-TENG on the FEP film, both the watch and calculator can work continuously without any auxiliary electronic equipment (Videos S1 and S2, ESI[†]). It is worth noting that the direct drive method makes the operation very simple and convenient, which well fits our living habits. Moreover, 99 commercial bulbs can be lit up by manually sliding the FDC-TENG, and the paper with the word “BINN” can be illuminated (Fig. 5d and e; Video S3, ESI[†]). This exhibits the high-power output performance and the potential for practical application of the FDC-TENG in our daily lives. Furthermore, 1053 LEDs (the threshold voltage of each LED is 3.0–3.2 V) can also be easily lit up, while no light can be observed after swapping the two electrodes. These indicate the high voltage and DC output characteristics of our FDC-TENG (Fig. 5f and g; Video S4, ESI[†]). In addition, only a few LEDs are lit up when the breakdown electrode is not connected, indicating a huge change after simply adding a breakdown electrode to the polyester–cotton fabric. To demonstrate the wearable feature, 96 heart-shaped colored lights sewn into a sweater are also lit up by manually sliding the FDC-TENG on the FEP film that is attached to the arm (Fig. 5h and i, Video S5, ESI[†]). As an energy harvester, the harvesting energy of the FDC-TENG can also be stored in capacitors for the subsequent utilization of high-power electronic devices, such as a hygromograph. The voltage curve of two 100 μF electrolytic capacitors in series is shown in Fig. 5j, and the insets display the overall operation photo and the circuit diagram. The stored electrical energy of the capacitors by manually sliding the FDC-TENG can successfully drive a hygromograph with the real-time display of temperature and humidity (Video S6, ESI[†]). These demonstrations of our FDC-TENG illustrate its broad application prospects in our daily lives.

Conclusions

In summary, we have developed a high-power output, fully flexible, light weight, and wearable FDC-TENG by simply and easily coating silver paste on the top and bottom sides of a polyester–cotton fabric for energy harvesting. Various structural parameters and external factors are deeply explored for in-depth understanding of the FDC-TENG based on the

coupling effect of triboelectrification and air breakdown. The increased sliding speed will linearly increase the magnitude of current and voltage, but has an enhanced effect on the charge transfer only at low speeds ($< 0.05 \text{ m s}^{-1}$), due to the nonnegligible dissipation of charges. The electrical output performance will severely decrease with the increase of relative humidity. Furthermore, the electrical output can be multiplied by increasing the number of breakdown electrodes and integrated units. To verify the practical application potential and high output of the FDC-TENG, 99 commercial bulbs, 1053 LEDs, and 96 heart-shaped colored lights can be lit up easily. Low-power wearable electronics, such as watches and calculators, can also be easily and directly driven without either rectifying or capacitor charging. This work may not only promote human biomechanical energy harvesting for wearable electronics in the era of IoT, but also provide a novel design concept for DC high output power fabrics.

Experimental

Fabrication of an FDC-TENG

The preparation of an FDC-TENG is extremely simple and easy. It involved using a tiny scraper to coat conductive silver paste on the bottom side of a polyester–cotton fabric as a friction electrode, followed by drying it in an oven at 120 $^{\circ}\text{C}$ for 20 min. Then the above operation was repeated on the top side of the polyester–cotton fabric as a breakdown electrode. The two electrodes should not overlap to prevent them from conducting.

Characterization and measurements

The FDC-TENG was driven using a linear motor (LinMot E1200) for electrical measurements, and the I_{SC} and Q_{SC} were measured using an electrometer (Keithley, model 6514), while the voltage was gauged using an oscilloscope (Tektronix, MDO3024) with a high-voltage probe (HVP 3015, 1/1000, 500 M Ω). The surface potential of the FEP film was tested using an Isoprobe electrostatic voltmeter (model 279). The backside resistance of a friction electrode was measured using an electrometer (Keithley, model 6517B). The breathability of the fabrics was measured using an Air Permeability Tester (TQD-G1).

Author contributions

R. C. and K. D. conceived the idea. K. D. and Z. L. W. supervised the experiment. R. C. and K. D. performed the experiment and the data analyses and wrote the manuscript. P. C., C. N., X. P., Y. Z., and D. L. helped perform the experiment and the analysis with constructive discussions. All the authors discussed the results and commented on the manuscript.

Conflicts of interest

The authors declare no conflicts of interest.

Acknowledgements

The authors are grateful for the support received from the National Key R&D Project from the Ministry of Science and Technology (Grant No. 2016YFA0202704), the Beijing Municipal Natural Science Foundation (Grant No. 2212052), the Shanghai Sailing Program (Grant No. 19S28101) and the Fundamental Research Funds for the Central Universities (Grant No. 19D128102).

References

- B. Dunn, H. Kamath and J.-M. Tarascon, Electrical Energy Storage for the Grid: A Battery of Choices, *Science*, 2011, **334**, 928–935.
- H. Sun, Y. Zhang, J. Zhang, X. Sun and H. Peng, Energy Harvesting and Storage in 1D Devices, *Nat. Rev. Mater.*, 2017, **2**, 17023.
- K. Shum and A. Tsatskina, Solar Cells: Stabilizing Tin-Based Perovskites, *Nat. Energy*, 2016, **1**, 16188.
- S. Hong, Y. Gu, J. K. Seo, J. Wang, P. Liu, Y. S. Meng, S. Xu and S. Chen, Wearable Thermoelectrics for Personalized Thermoregulation, *Sci. Adv.*, 2019, **5**, eaaw0536.
- H. Guo, X. Pu, J. Chen, Y. Meng, M.-H. Yeh, G. Liu, Q. Tang, B. Chen, D. Liu, S. Qi, C. Wu, C. Hu, J. Wang and Z. L. Wang, A Highly Sensitive, Self-Powered Triboelectric Auditory Sensor for Social Robotics and Hearing Aids, *Sci. Rob.*, 2018, **3**, eaat2516.
- R. Cheng, K. Dong, L. Liu, C. Ning, P. Chen, X. Peng, D. Liu and Z. L. Wang, Flame-Retardant Textile-Based Triboelectric Nanogenerators for Fire Protection Applications, *ACS Nano*, 2020, **14**, 15853–15863.
- K. Dong, X. Peng, J. An, A. C. Wang, J. Luo, B. Sun, J. Wang and Z. L. Wang, Shape Adaptable and Highly Resilient 3D Braided Triboelectric Nanogenerators as E-Textiles for Power and Sensing, *Nat. Commun.*, 2020, **11**, 2868.
- W. Gong, C. Hou, J. Zhou, Y. Guo, W. Zhang, Y. Li, Q. Zhang and H. Wang, Continuous and Scalable Manufacture of Amphibious Energy Yarns and Textiles, *Nat. Commun.*, 2019, **10**, 868.
- C. Ning, K. Dong, R. Cheng, J. Yi, C. Ye, X. Peng, F. Sheng, Y. Jiang and Z. L. Wang, Flexible and Stretchable Fiber-Shaped Triboelectric Nanogenerators for Biomechanical Monitoring and Human-Interactive Sensing, *Adv. Funct. Mater.*, 2020, **31**, 2006679.
- X. Peng, K. Dong, C. Ye, Y. Jiang, S. Zhai, R. Cheng, D. Liu, X. Gao, J. Wang and Z. L. Wang, A Breathable, Biodegradable, Antibacterial, and Self-Powered Electronic Skin Based on All-Nanofiber Triboelectric Nanogenerators, *Sci. Adv.*, 2020, **6**, eaba9624.
- K. Dong, J. Deng, Y. Zi, Y. C. Wang, C. Xu, H. Zou, W. Ding, Y. Dai, B. Gu, B. Sun and Z. L. Wang, 3D Orthogonal Woven Triboelectric Nanogenerator for Effective Biomechanical Energy Harvesting and as Self-Powered Active Motion Sensors, *Adv. Mater.*, 2017, **29**, 1702648.
- C. Dong, A. Leber, T. Das Gupta, R. Chandran, M. Volpi, Y. Qu, T. Nguyen-Dang, N. Bartolomei, W. Yan and F. Sorin, High-Efficiency Super-Elastic Liquid Metal Based Triboelectric Fibers and Textiles, *Nat. Commun.*, 2020, **11**, 3537.
- Y. Jiang, K. Dong, X. Li, J. An, D. Wu, X. Peng, J. Yi, C. Ning, R. Cheng, P. Yu and Z. L. Wang, Stretchable, Washable, and Ultrathin Triboelectric Nanogenerators as Skin-Like Highly Sensitive Self-Powered Haptic Sensors, *Adv. Funct. Mater.*, 2020, 2005584.
- Y.-C. Lai, J. Deng, S. L. Zhang, S. Niu, H. Guo and Z. L. Wang, Single-Thread-Based Wearable and Highly Stretchable Triboelectric Nanogenerators and Their Applications in Cloth-Based Self-Powered Human-Interactive and Biomedical Sensing, *Adv. Funct. Mater.*, 2017, **27**, 1604462.
- R. Cao, X. Pu, X. Du, W. Yang, J. Wang, H. Guo, S. Zhao, Z. Yuan, C. Zhang, C. Li and Z. L. Wang, Screen-Printed Washable Electronic Textiles as Self-Powered Touch/Gesture Tribo-Sensors for Intelligent Human-Machine Interaction, *ACS Nano*, 2018, **12**, 5190–5196.
- K. Dong, Z. Wu, J. Deng, A. C. Wang, H. Zou, C. Chen, D. Hu, B. Gu, B. Sun and Z. L. Wang, A Stretchable Yarn Embedded Triboelectric Nanogenerator as Electronic Skin for Biomechanical Energy Harvesting and Multifunctional Pressure Sensing, *Adv. Mater.*, 2018, **30**, e1804944.
- H. Guo, Z. Wen, Y. Zi, M.-H. Yeh, J. Wang, L. Zhu, C. Hu and Z. L. Wang, A Water-Proof Triboelectric-Electromagnetic Hybrid Generator for Energy Harvesting in Harsh Environments, *Adv. Energy Mater.*, 2016, **6**, 1501593.
- L. Xu, T. Jiang, P. Lin, J. J. Shao, C. He, W. Zhong, X. Y. Chen and Z. L. Wang, Coupled Triboelectric Nanogenerator Networks for Efficient Water Wave Energy Harvesting, *ACS Nano*, 2018, **12**, 1849–1858.
- Z. Wu, H. Guo, W. Ding, Y. C. Wang, L. Zhang and Z. L. Wang, A Hybridized Triboelectric-Electromagnetic Water Wave Energy Harvester Based on a Magnetic Sphere, *ACS Nano*, 2019, **13**, 2349–2356.
- A. Li, Y. Zi, H. Guo, Z. L. Wang and F. M. Fernandez, Triboelectric Nanogenerators for Sensitive Nano-Coulomb Molecular Mass Spectrometry, *Nat. Nanotechnol.*, 2017, **12**, 481–487.
- J. Cheng, W. Ding, Y. Zi, Y. Lu, L. Ji, F. Liu, C. Wu and Z. L. Wang, Triboelectric Microplasma Powered by Mechanical Stimuli, *Nat. Commun.*, 2018, **9**, 3733.
- H. Guo, J. Chen, L. Wang, A. C. Wang, Y. Li, C. An, J.-H. He, C. Hu, V. K. S. Hsiao and Z. L. Wang, A Highly Efficient Triboelectric Negative Air Ion Generator, *Nat. Sustainable*, 2021, **4**, 147–153.
- K. Dong, X. Peng and Z. L. Wang, Fiber/Fabric-Based Piezoelectric and Triboelectric Nanogenerators for Flexible/Stretchable and Wearable Electronics and Artificial Intelligence, *Adv. Mater.*, 2020, **32**, e1902549.
- K. Meng, S. Zhao, Y. Zhou, Y. Wu, S. Zhang, Q. He, X. Wang, Z. Zhou, W. Fan, X. Tan, J. Yang, J. Chen and A. Wireless, Textile-Based Sensor System for Self-Powered Personalized Health Care, *Matter*, 2020, **2**, 896–907.
- Z. Zhou, K. Chen, X. Li, S. Zhang, Y. Wu, Y. Zhou, K. Meng, C. Sun, Q. He, W. Fan, E. Fan, Z. Lin, X. Tan, W. Deng, J. Yang and J. Chen, Sign-to-Speech Translation Using

- Machine-Learning-Assisted Stretchable Sensor Arrays, *Nat. Electron.*, 2020, **3**, 571–578.
- 26 G. Chen, Y. Li, M. Bick and J. Chen, Smart Textiles for Electricity Generation, *Chem. Rev.*, 2020, **120**, 3668–3720.
- 27 Z. L. Wang, Entropy Theory of Distributed Energy for Internet of Things, *Nano Energy*, 2019, **58**, 669–672.
- 28 J. Liu, A. Goswami, K. Jiang, F. Khan, S. Kim, R. McGee, Z. Li, Z. Hu, J. Lee and T. Thundat, Direct-Current Triboelectricity Generation by a Sliding Schottky Nanocontact on MoS₂ Multilayers, *Nat. Nanotechnol.*, 2018, **13**, 112–116.
- 29 R. Lei, Y. Shi, Y. Ding, J. Nie, S. Li, F. Wang, H. Zhai, X. Chen and Z. L. Wang, Sustainable High-Voltage Source Based on Triboelectric Nanogenerator with a Charge Accumulation Strategy, *Energy Environ. Sci.*, 2020, **13**, 2178–2190.
- 30 S. Jung, J. Lee, T. Hyeon, M. Lee and D. H. Kim, Fabric-based integrated energy devices for wearable activity monitors, *Adv. Mater.*, 2014, **26**, 6329–6334.
- 31 Z. Wen, M.-H. Yeh, H. Guo, J. Wang, Y. Zi, W. Xu, J. Deng, L. Zhu, X. Wang, C. Hu, L. Zhu, X. Sun and Z. L. Wang, Self-Powered Textile for Wearable Electronics by Hybridizing Fiber-Shaped Nanogenerators, Solar Cells, and Supercapacitors, *Sci. Adv.*, 2016, **2**, e1600097.
- 32 J. Xiong, M.-F. Lin, J. Wang, S. L. Gaw, K. Parida and P. S. Lee, Wearable All-Fabric-Based Triboelectric Generator for Water Energy Harvesting, *Adv. Energy Mater.*, 2017, **7**, 1701243.
- 33 C. Ning, L. Tian, X. Zhao, S. Xiang, Y. Tang, E. Liang and Y. Mao, Washable textile-structured single-electrode triboelectric nanogenerator for self-powered wearable electronics, *J. Mater. Chem. A*, 2018, **6**, 19143–19150.
- 34 C. Chen, H. Guo, L. Chen, Y. C. Wang, X. Pu, W. Yu, F. Wang, Z. Du and Z. L. Wang, Direct Current Fabric Triboelectric Nanogenerator for Biomotion Energy Harvesting, *ACS Nano*, 2020, **14**, 4585–4594.
- 35 J. Gong, B. Xu, X. Guan, Y. Chen, S. Li and J. Feng, Towards Truly Wearable Energy Harvesters with Full Structural Integrity of Fiber Materials, *Nano Energy*, 2019, **58**, 365–374.
- 36 C. Chen, L. Chen, Z. Wu, H. Guo, W. Yu, Z. Du and Z. L. Wang, 3D Double-Faced Interlock Fabric Triboelectric Nanogenerator for Bio-Motion Energy Harvesting and as Self-Powered Stretching and 3D Tactile Sensors, *Mater. Today*, 2020, **32**, 84–93.
- 37 D. Liu, L. Zhou, S. Li, Z. Zhao, X. Yin, Z. Yi, C. Zhang, X. Li, J. Wang and Z. L. Wang, Hugely Enhanced Output Power of Direct-Current Triboelectric Nanogenerators by Using Electrostatic Breakdown Effect, *Adv. Mater. Technol.*, 2020, **5**, 2000289.
- 38 K. Lee, J. Chun, J. Lee, K. Kim, N. Kang, J. Kim, M. Kim, K. Shin, M. Gupta, J. Baik and S. W. Kim, Hydrophobic Sponge Structure-Based Triboelectric Nanogenerator, *Adv. Mater.*, 2014, **26**, 5037–5042.
- 39 R. Wen, J. Guo, A. Yu, J. Zhai and Z. L. Wang, Humidity-Resistive Triboelectric Nanogenerator Fabricated Using Metal Organic Framework Composite, *Adv. Funct. Mater.*, 2019, **29**, 1807655.
- 40 K. Dong, Y. C. Wang, J. Deng, Y. Dai, S. L. Zhang, H. Zou, B. Gu, B. Sun and Z. L. Wang, A Highly Stretchable and Washable All-Yarn-Based Self-Charging Knitting Power Textile Composed of Fiber Triboelectric Nanogenerators and Supercapacitors, *ACS Nano*, 2017, **11**, 9490–9499.
- 41 C. Wu, A. C. Wang, W. Ding, H. Guo and Z. L. Wang, Triboelectric Nanogenerator: A Foundation of the Energy for the New Era, *Adv. Energy Mater.*, 2019, **9**, 1802906.
- 42 B. Li, X. Li, M. Fu, R. Zhuo and D. Wang, Effect of Humidity on Dielectric Breakdown Properties of Air Considering Ion Kinetics, *J. Phys. D*, 2018, **51**, 375201.
- 43 G. Zhu, Y. Su, P. Bai, J. Chen, Q. Jing, W. Yang and Z. L. Wang, Harvesting Water Wave Energy by Asymmetric Screening of Electrostatic Charges on a Nanostructured Hydrophobic Thin-Film Surface, *ACS Nano*, 2014, **8**, 6031–6037.
- 44 Y. Cho, K. Lee, S. Park, S. Ahn, W. Kim, J. Kim, S. Park, J. Sun, C. Jung, J. Chung, M. Chang, D. Choi and J.-J. Park, Rotational wind power triboelectric nanogenerator using aerodynamic changes of friction area and the adsorption effect of hematoxylin onto feather based on a diversely evolved hyper-branched structure, *Nano Energy*, 2019, **61**, 370–380.
- 45 Z. Ren, Z. Wang, Z. Liu, L. Wang, H. Guo, L. Li, S. Li, X. Chen, W. Tang and Z. L. Wang, Energy Harvesting from Breeze Wind (0.7–6 m s⁻¹) Using Ultra-Stretchable Triboelectric Nanogenerator, *Adv. Energy Mater.*, 2020, **10**, 2001770.
- 46 D. Liu, X. Yin, H. Guo, L. Zhou, X. Li, C. Zhang, J. Wang and Z. L. Wang, A Constant Current Triboelectric Nanogenerator Arising from Electrostatic Breakdown, *Sci. Adv.*, 2019, **5**, eaav6437.